Article

In Situ DRIFTS Study of Single-Atom, 2D, and 3D Pt on γ-Al$_2$O$_3$ Nanoflakes and Nanowires for C$_2$H$_4$ Oxidation

Shengpan Peng [1,†] , Ziran Ma [1,†] , Jing Ma [1] , Hongyan Wang [1] , Kai Ren [1] , Xiaodong Wu [2]
and Baodong Wang [1,*]

1   National Institute of Clean-and-Low-Carbon Energy, Beijing 102211, China
2   Key Laboratory of Advanced Materials of Ministry of Education, School of Materials Science and Engineering,
    Tsinghua University, Beijing 100084, China
*   Correspondence: baodong.wang.d@chnenergy.com.cn; Tel.: +86-010-57339633
†   These authors contributed equally to this work.

Abstract: Up to now, a great number of catalysts have been reported that are active in the oxidation of volatile organic compounds (VOCs). However, supported noble-metal catalysts (especially Pt-based catalysts) are still the most excellent ones for this reaction. In this study, Pt species supported on γ-Al$_2$O$_3$ and ranging from single-atom sites to clusters (less than 1 nm) and 1–2 nm nanoparticles were prepared and investigated for oxidizing C$_2$H$_4$. The Pt-loaded γ-Al$_2$O$_3$ nanoflakes (PtAl-NF) and Pt-loaded γ-Al$_2$O$_3$ nanowires (PtAl-NW) were successfully prepared. The samples were characterized using XRD, TEM, XPS, HAADF-STEM, and in situ DRIFTS. Based on in situ DRIFTS, a simple surface reaction mechanism was developed. The stable intermediates CO on single-atom Pt, subnanometer Pt particles, and fully exposed Pt clusters could be explained by the strong binding of CO molecule poisoning Pt sites. Moreover, the oxidation of C$_2$H$_4$ was best achieved by Pt particles that were 1–2 nm in size and the catalytic activity of PtAl-NF was better when it had less Pt. Lastly, the most exposed (110) facets of γ-Al$_2$O$_3$ nanoflakes were more resistant to water than the majorly exposed (100) facets of γ-Al$_2$O$_3$ nanowires.

Keywords: in situ DRIFTS; supported Pt catalysts; size effects; C$_2$H$_4$ oxidation; surface reaction mechanism

1. Introduction

Volatile organic compounds (VOCs) are a major cause of air pollution because more and more factories and cities have created many places where VOCs can be released [1,2]. For example, petroleum refining [3], the pharmaceutical industry [4], the production of organic chemical materials [5], spraying, and printing [6] would all make alkanes, alkenes, alkynes, aromatics, halocarbons, and compounds with oxygen, sulfur, and nitrogen. Since a stricter clean air policy has been put into place recently, there has been a lot of focus on reducing VOCs [7]. Catalytic decomposition of VOCs is a good way to reduce air pollution that is also affordable [8,9]. Most of the time, noble metal catalysts on supports and transition metal oxides were used to get rid of VOCs [10–14]. Because they work better as catalysts, supported noble metal catalysts have been used a lot to get rid of VOC streams [15–17]. For example, Pt-based catalysts are very good at getting rid of lower hydrocarbons like C$_2$H$_4$, which could lead to full oxidation at temperatures below 200 °C [13].

Noble metals are expensive in trade markets and have a very limited available quantity, which thereby limits their use [18]. As active phases with a higher number of exposed noble metal atoms frequently exhibit a higher activity [19,20], noble metal particle sizes typically determine the ratio of the number of exposed noble metal atoms to the overall number. A lot of focus has been placed recently on single-atom catalysts (SACs) and fully exposed clusters (FECs), in which all of the noble metal atoms are exposed on the support surface.

The isolated noble metal structure of SACs catalysts, such as Pt_1/Al_2O_3 [21], Pt_1/FeO_x [22], Pt_1/CeO_2 [23], and Pt_1/TiO_2 [24], show high activity for CO oxidation. It should be kept in mind that ensembled noble metal sites with complete dispersion allow for a higher activity than SACs since isolated noble metal atoms without ensemble sites are unable to perform essential surface reactions that demand metal proximity [25]. This indicates that not all catalytic reactions can be efficiently catalyzed by a noble metal atom that has been dispersed 100% on support. On the one hand, the sensitivity of the reaction's molecular structure to single atoms, clusters, and particles would vary [25,26]. Contrarily, chemical valence would be controlled by size (single-atom and cluster states display cationic states, and particles generally show metallic states), which are necessary for dissociation and/or creation of target chemical bonds [27].

In this study, the valence states and structural sensitivity of supported Pt species—from single-atom sites to clusters (sub 1 nm) and 1–2 nm nanoparticles—were examined for the C_2H_4 oxidation. First, nanowire γ-alumina (γ-Al_2O_3) and nanoflake γ-alumina (γ-Al_2O_3) were fabricated; the respective exposed surfaces of these two types of alumina were primarily (100) and (110) facets. Second, various Pt species were seen when the same Pt loading (1 weight %) was applied to nanowire and nanoflake γ-Al_2O_3. The catalytic activity of single-atom, cluster, and nanoparticle Pt was confirmed by combining electron microscopy, in-situ DRIFTS, and X-ray photoelectron spectroscopy. The lower CO desorption and catalyst inactivation rates of single-atom Pt or Pt clusters revealed them ineffective for C_2H_4 oxidation. Instead, the 1–2 nm nanoparticles reflected the lower binding energy of Pt, permitting easy CO desorption, and were the most active Pt species for C_2H_4 oxidation.

2. Material and Methods

2.1. Materials

All chemical reagents were used as received without purification. $Pt(NO_3)_2$ solution (15 wt.% Pt) was supplied by (Shanghai Jiuling Chemical Co., Ltd., Shanghai, China) $Al(NO_3)_3 \cdot 9H_2O$ (Chemically Pure), NaOH (Chemically Pure), $NaAlO_2$ (Chemically Pure), and $AlCl_3 \cdot 6H_2O$ (Analytical Reagent) were purchased from (Sinopharm Chemical Reagent Co., Ltd., Shanghai, China).

2.2. γ-Al_2O_3 Nanoflake (Al-NF) Preparation [28]

Dropwise additions of 1 M NaOH solution were added to the agitated 0.25 M $Al(NO_3)_3$ solution until the pH of the mixture reached 10. $Al(OH)_3$ gel was produced after 1 h of room temperature ageing. Then, a 200 mL Teflon container with the mixture (160 mL) inside was sealed within a steel vessel. The container was heated on a Muffle furnace for 48 h at 200 °C. The solid white result underwent four cycles of centrifugation and deionized water washing. For 12 h, the solid sample was dried at 120 °C. The final products are ground to a particle size of less than 100 μm and then calcined in air for five hours at 550 °C with a 5 °C per minute heating ramp. The sample was named Al-NF.

2.3. γ-Al_2O_3 Nanowire (Al-NW) Preparation [29]

The stirred 0.25 M $Al(NO_3)_3$ solution received 0.4 M $NaAlO_2$ solution (72 mL). $Al(OH)_3$ gel was produced after 1 h of room temperature ageing. Then, the mixture was poured into a 200 mL Teflon container and placed within a steel vessel before being sealed. The container was heated on a Muffle furnace for 24 h at 150 °C. The solid white result underwent four cycles of centrifugation and deionized water washing. For 12 h, the solid sample was dried at 120 °C. The final products are ground to a particle size of less than 100 μm and then calcined in air for five hours at 550 °C with a 5 °C per minute heating ramp. The sample was named Al-NW.

2.4. 1 wt.% Pt/Al_2O_3 Preparation

In 5 mL of distilled water, 200 mg of $Pt(NO_3)_2$ solution (15 wt.% as Pt) was added (solution A). 2.97 g of support (Al-NF and Al-NW) from Solution A were combined to make a viscous slurry, which was then evaporated on a hot plate to almost dryness (while stirring continually) and dried for 12 h at 120 °C. The finished products were ground to a particle size of less than 100 μm and calcined in air for five hours at 550 °C with a 5 °C per minute heating ramp. All Pt-loaded samples were named PtAl-NF and PtAl-NW.

2.5. Characterization Techniques

JEM-ARM200F (JEOL, Tokyo, Japan) operated at a 200 kV accelerating voltage to produce the images for transmission electron microscopy (TEM, Tokyo, Japan) and high-angle annular dark-field scanning transmission electron microscopy (HAADF-STEM, Tokyo, Japan). A tiny sample was equally disseminated in ethanol, put on a Cu grid covered with carbon, and dried for characterization. X-ray photoelectron spectroscopy (XPS) was used to investigate the electrical characteristics of Pt (Al K-alpha, Thermo Scientific, ESCALAB 250Xi, Waltham, MA, USA). The reference point for estimating the binding energies of the Pt element was the maximal strength of the beneficial C 1s signal at 284.8 eV. Powder X-ray diffraction (PXRD, Bruker D8 ADVANCE, Billerica, MA, USA) with monochromatic CuKa radiation (λ_{CuKa} = 1.54056 Å) was used to reveal structural analyses. The gas absorption technique Brunauer-Emmett-Teller (BET, Micromeritics®, Norcross, GA, USA) was employed for the determination of the surface area of samples. Surface area measurements were performed using N_2 gas at a temperature of 77 K. To remove physisorbed species from the surface, samples were degassed at 150 °C under a vacuum for 24 h. Pore size distribution and pore volume were determined by BJH analysis.

Diffuse reflectance infrared Fourier transform spectroscopy (DRIFTS) experiments were performed on a BRUKER VERTEX 70 FTIR spectrometer equipped with a liquid-nitrogen cooled mercury-cadmium-telluride (MCT) detector. Samples (17 mg) were put into the reaction chamber. The loaded samples were then warmed for 30 min at 400 °C with pure Ar (50 mL min^{-1}). Catalyst background spectra were obtained using Fourier transform infrared spectroscopy (FTIR) when the chamber was cooled to 180 °C, 160 °C, 140 °C, and 120 °C. The chamber was first brought to 120 °C, then allowed to cool to ambient temperature. 50 mL min^{-1} of mixed gas (10 mL min^{-1} O_2, 35 mL min^{-1} N_2, and 5 mL min^{-1} 0.7% C_2H_4/N_2) was added to the system to replace the pure Ar. At a resolution of 4 cm^{-1}, an average of 128 scans were used to gather all the spectra. The chamber was heated to 140 °C in the Ar environment after 10 min. Following a 30-min Ar purge, the chamber was filled with the mixed gas, and spectra were once more obtained. The same method was used to obtain data at 160 °C and 180 °C.

Then, in a PIKE® infrared cell provided with a regulated environment and temperature, in situ DRIFTS was carried out on PtAl-NF and PtAl-NW to examine the evolution of surface species on catalysts under C_2H_4 oxidation conditions (Figure 1). The less specular and more diffuse the reflection component is, the smaller the sample particle is, and the more sensitive the measurement is. Particle sizes in the diffuse reflection sample ranged from 2 to 5 μm. As shown in Figure 1, after inserting the sample into the crucible, gently flatten the powder with a metal rod to increase the compact sample's specular reflection component. The sample was also placed in an in-situ cell that has been warmed to 400 °C. After cooling to a specific temperature, the sample was purged with argon gas for one hour, and the background spectrum was measured.
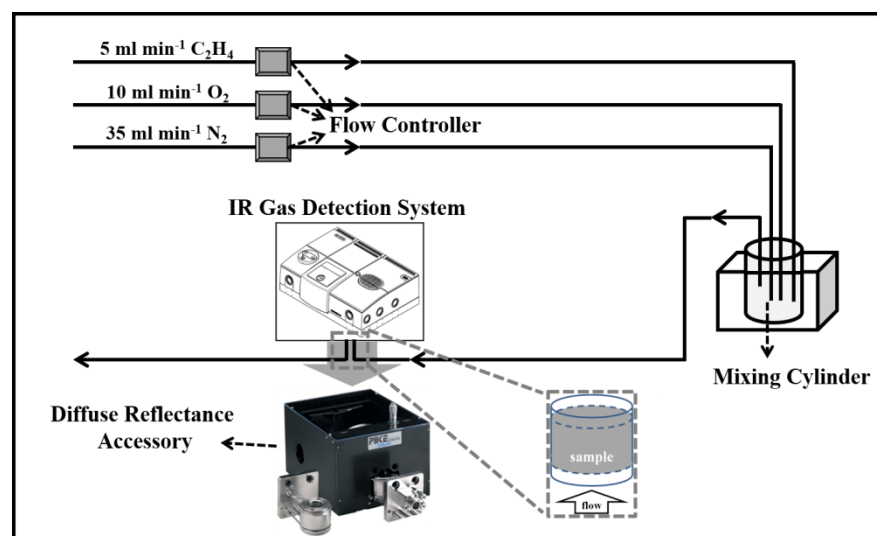
Figure 1. The testing system of in situ diffuse reflectance FT−IR spectroscopy.

2.6. Catalytic Activity Tests

All the tests were conducted at 0.1 atm. C_2H_4 oxidation experiments were carried out in a tube micro-reactor with an internal diameter of 13 mm. The catalyst (100 mg Catalyst + 400 mg quartz sand) was sieved between 40–60 grain size mesh and shifted into the reactor with a bed volume of around 0.5 mL, between two layers of quartz wool, which functions to avoid catalyst powder displacement while also pre-heating the reagents. The reactor was heated using the oven, and the temperature of the catalyst was monitored using a K-type thermocouple put within the reactor, close to the catalytic bed.

The composition of the reactant mixture was adjusted by adjusting the flow rates of C_2H_4, O_2, and N_2, meanwhile keeping the overall flow rate constant at 1000 mLmin^{-1}. The conditions were consistent with a gas hourly space velocity (GHSV) of 600,000 mL g$_{cat.}$$^{-1}$ h^{-1}. The composition of the effluent gases was monitored online using a Fourier-transform infrared (FT-IR) gas analyzer (MKS, MultiGas^{TM} analyzer, model 6030) equipped with a liquid-nitrogen cooled mercury-cadmium-telluride (MCT) detector. The cut-off wavelength for the detector was 16 μm, the window type was ZnSe, the detector size was 0.25 mm, and the path length was 5.11 m.

3. Results and Discussion

3.1. Characterizations of Pt/Al$_2$O$_3$ Catalysts

3.1.1. Characterizations of Al$_2$O$_3$ Supports

XRD characterizations were carried out for analysis of the crystalline structures of Al$_2$O$_3$ obtained following the calcination of boehmite (Figure 2). It is evident from the XRD profiles that crystallized γ-Al$_2$O$_3$ was successfully prepared and the obtained data matches well with the JCPDS powder diffraction pattern 10-0425. The diffraction peaks appeared at 2θ = 19.5°, 37.6°, 39.5°, 45.9°, 60.8°, and 67.1° indexed to (111), (220), (311), (222), (400), (511), and (440), which indicated that there were no diffraction peaks attributed to Al(OH)$_3$ or γ-AlOOH phases [30,31]. The crystal size of γ-Al$_2$O$_3$ samples can be determined by Scherrer's equation from the XRD (440) peaks (Equation (1)).

$$D = k\lambda 57.3 / [L_{FWHM} cos\theta] \tag{1}$$

where D is crystal size in the direction perpendicular to the lattice planes, k is a constant with a value of 0.9, λ refers to the wavelength of the X-rays, L_{FWHM} is the width at half the maximum of peaks, and θ stands for the Bragg angle. The crystalline sizes were calculated using equation 1, and the crystal size of Al-NF and Al-NW were respectively determined as 10.8 nm and 8.4 nm. The thickness of Al-NF was about 30–50 nm (Figure S1), which was

not consistent with the crystal size derived from XRD (440) peak. The differences may be attributed to the existence of nanoflakes in sample Al-NF as aggregated crystalline grains with sizes of around 10 nm, which fused to form nanoflakes. Furthermore, Figure S2 clearly showed that the uneven zigzag edges of nanoflakes were comprised of small and uniform grains (10 nm). As shown in Figure S3, the diameter of Al-NW was almost identical to the crystal size deduced from XRD (440) peaks, which suggested an uninterrupted growth of the crystal size in the (110) direction.
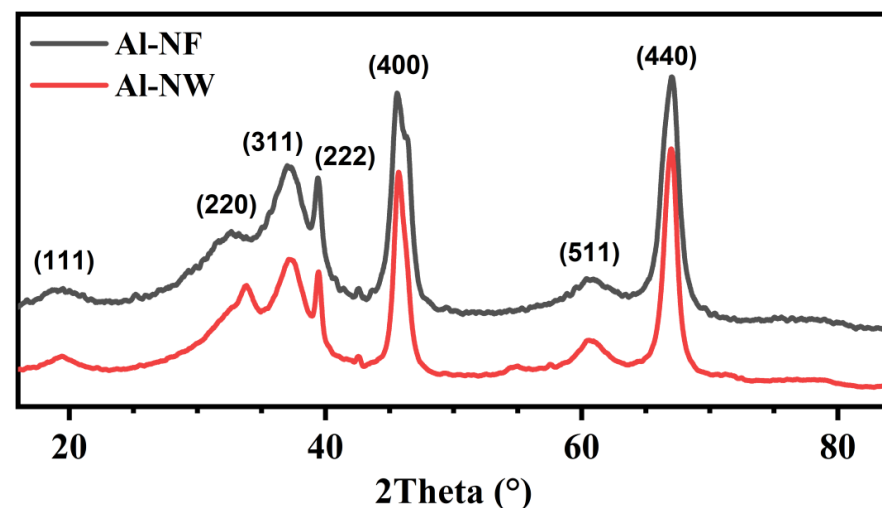

Figure 2. XRD patterns of synthesized nanoflake (Al-NF) and nanowire (Al-NW) γ-Al$_2$O$_3$.

HRTEM observations were subsequently carried out to confirm the microstructural characteristics of the γ-Al$_2$O$_3$ samples which were earlier inferred from the XRD patterns. The sample prepared in part 2.2 using Al^{3+}/AlO$_2^-$ exhibited highly distributed γ-AlOOH-based nanoflakes. After calcination at 550 °C, γ-AlOOH transformed into γ-Al$_2$O$_3$ [32–34], and the TEM image of γ-Al$_2$O$_3$ nanoflake (Al-NF) has been depicted in Figure 3a. The lengths and thickness of the as-prepared Al-NF were about 200 nm and 40 nm, respectively. Besides, the developed nanoflakes manifested straight edges with angles measuring 76° and 104°, which corresponded to the angle between the (101) and (−101) faces of γ-AlOOH [28,29,35], indicating γ-AlOOH nanoflakes grew with basal planes and lateral faces of (010) and (101). The Al-NF therefore directly inherited the morphology of γ-AlOOH nanoflakes and the exposed γ-AlOOH faces (010) and (101) were converted to basal planes and lateral faces of (110) and (111) of γ-Al$_2$O$_3$ by topological rules [36,37]. The highly magnified TEM image of the γ-Al$_2$O$_3$ nanoflake has been shown in Figure 3c. The lattice fringes of Al-NF with a *d*-spacing of 0.225 nm, corresponding to the (110) plane of γ-Al$_2$O$_3$, can be observed clearly [38]. The protocol described in part 2.3 produced γ-Al$_2$O$_3$ nanowires (Al-NW) as shown in Figure 3b. The lengths and diameters of the as-prepared Al-NW were observed to be 100 nm and 10 nm, respectively. Figure 3d is a representation of HRTEM images where lattice fringes attributed to (100) planes of the γ-Al$_2$O$_3$ phase, can be observed.
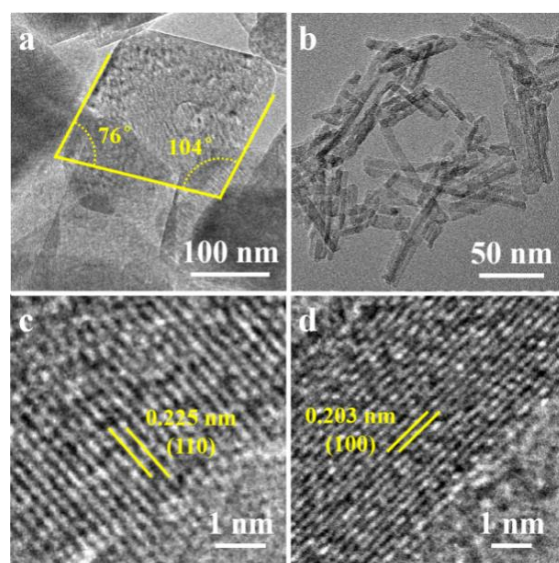
Figure 3. High-resolution TEM images of synthesized γ-Al$_2$O$_3$. (**a**,**c**) Al-NF and (**b**,**d**) Al-NW.

3.1.2. Characterizations of Pt Supported on γ-Al$_2$O$_3$

Pt-loaded γ-Al$_2$O$_3$ samples were synthesized with different γ-Al$_2$O$_3$ supports (PtAl-NF and PtAl-NW) as shown in Table 1. The final concentration of Pt on the support was 1 wt.% for all syntheses. Elemental analysis was carried out to investigate the Pt content. A similar specific surface area, as shown in Table 1, was standard for indifferent effects on Pt dispersion. Moreover, the similar pore volume and average pore size eliminated the variation of mass transfer rate. Thus, the difference between PtAl-NF and PtAl-NW exposed the crystal planes, thus leading to different Pt structures and dispersions.

Table 1. The concentration of Pt Present on γ-Al$_2$O$_3$ and BET Surface Area.

Catalyst	Surface Area/m$^2 \cdot$g^{-1}	Pore Volume/mL$\cdot$g^{-1}	Average Pore Diameter/nm	Pt Loading/wt.%
PtAl-NF	66.7	0.27	15.8	0.98
PtAl-NW	76.4	0.32	16.3	0.97

3.2. Catalytic Activity of PtAl-NF and PtAl-NW

Catalytic conversion of C$_2$H$_4$ using PtAl-NF was accomplished at around 240 °C, using a gas stream containing 0.07% C$_2$H$_4$ and 10% O$_2$ in N$_2$ at a space of 600,000 mL g$_{cat.}^{-1}$ h^{-1} (Figure 4). By comparison, the reference sample (PtAl-NW) achieved 80% C$_2$H$_4$ conversion, which was 20% lower than the PtAl-NF catalyst at 240 °C. Pt has been accepted as the active phase in this reaction, in which γ-Al$_2$O$_3$ only served as a carrier and had no involvement in catalysis [13]. In the range of reaction temperature, C$_2$H$_4$ oxidation and O$_2$ activation on different Pt sites at Pt/Al$_2$O$_3$ interface occur through a redox or Mars-Van Krevelen (MvK) mechanism where the lattice O was consumed during the catalyst reduction step accompanied by the oxidation of the reactant, and this was followed by the catalyst re-oxidation step by its reaction with molecular O$_2$ [13]. On the one hand, the C$_2$H$_4$ molecule was absorbed on two adjacent Pt sites and formed a di-σ configuration (C$_2$H$_4$(2S)) [13,44]. Pt, on the other hand, activated O$_2$ to form reactive O species (Pt-O*) [39]. The formation of C$_2$H$_4$(2S) and Pt-O* resulted in effective C$_2$H$_4$ oxidation reaction pathways. It is noteworthy that when compared with PtAl-NF, PtAl-NW having a higher Pt dispersion demonstrated a lower catalytic activity (Figure 4), thereby indicating that Pt atom aggregation on the Pt/γ-Al$_2$O$_3$ catalysts was certainly responsible for the increased reactivity of PtAl-NF.
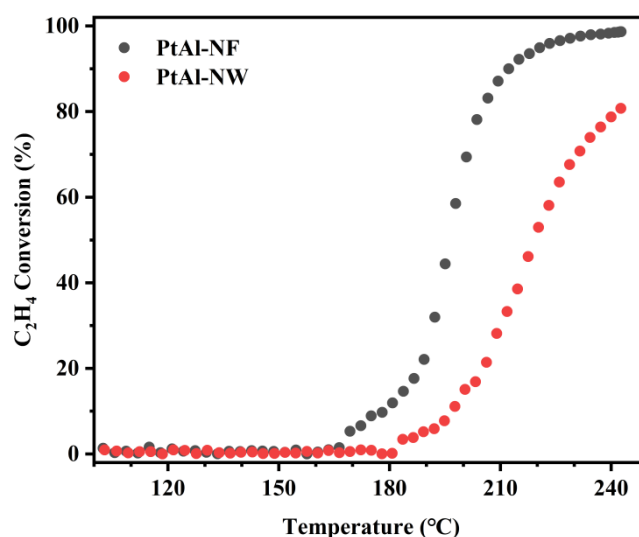
Figure 4. C_2H_4 combustion over a series of Pt (1 wt.%) catalysts at temperatures from 100 to 250 °C; Reaction conditions: 700 ppm C_2H_4, 10% O_2, N_2 balance, and GHSV = 600,000 mL $g_{cat.}^{-1}$ h^{-1}.

3.3. Development of Surface Reaction Model

Figure 5 depicts the experimental results of surface species measurement obtained by in situ DRIFTS, displaying the adsorption intensities of each surface species over the 1200–4000 cm^{-1} range. Broad IR bands in the 3390–3670 cm^{-1} range represent the adsorption due to the H_2O molecule [40,41], with the peak at 3700 cm^{-1} corresponding to Pt-OH species which showed a higher wavenumber than Al-OH. When the sample was switched from PtAl-NW to PtAl-NF, the IR bands of adsorbed H_2O began to decline under the same reaction conditions, whereas the Pt-OH peak vanished completely. This suggested that the γ-Al_2O_3 nanowires were more hydrophilic inducing the formation of Pt-OH species. As shown in Table 2, the R10 ($H_2O(S) \leftrightarrow H_2O + Pt(S)$) suggested that adsorption water on the support surface would decrease Pt active sites. The =C-H, -CH$_3$, and -CH$_2$ species were represented by the weak IR bands at 3130 cm^{-1}, 2950 cm^{-1}, and 2910 cm^{-1} respectively [13,42]. The dehydrogenation of C_2H_4 (2S) by the surface oxygen adsorbed during the reaction (Pt-O) is thought to be the origin of the creation of the -CH$_3$ and -CH$_2$ species. However, the =C-H species were not seen on the surface of PtAl-NF, indicating that the PtAl-NF catalyst might change =C-H species too quickly for them to be practically observable. The bands about 2350 cm^{-1} are most likely caused by CO_2 [13]. The detected peaks at around 2040 cm^{-1} and 2110 cm^{-1} were caused by CO species adsorbed linearly on the Pt [43–46]. While the peak at 2110 cm^{-1} indicated linearly adsorbed CO on small Pt particles or single-atom Pt, the peak at 2040 cm^{-1} indicated the existence of linearly adsorbed CO on Pt particles [44]. The PtAl-NW catalyst's CO absorption peak intensity was much higher than that of the PtAl-NF catalyst's, demonstrating the PtAl-superior NW's CO adsorption capability. Additionally, a bigger Pt dispersion in PtAl-NW was indicated by the peak's higher intensity at 2110 cm^{-1}, which is consistent with TEM data. The oxidation of the CH$_X$ species generated during the reaction may result in the formation of -COOH or -COO$^-$ (1600–1700 cm^{-1}) [47].
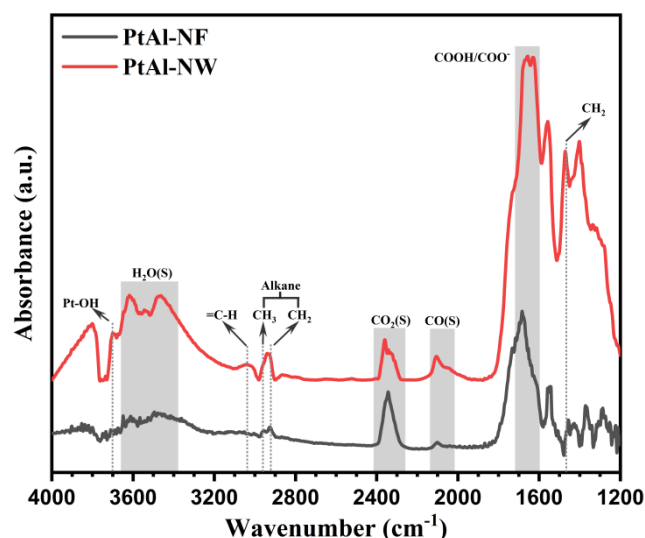
Figure 5. In situ DRIFT spectra over Pt/γ−Al$_2$O$_3$ at 180 °C. Reaction conditions: 700 ppm C$_2$H$_4$, 10% O$_2$, N$_2$ balance, 17 mg catalyst, and 50 mL min^{-1} flow rate.

Table 2. Proposed surface reaction steps of C$_2$H$_4$ for Pt/γ-Al$_2$O$_3$.

Reaction		
R1	O$_2$ + 2Pt(S) $\leftrightarrow$ 2O(S)	Reversible
R2	C$_2$H$_4$ + 2Pt(S) $\leftrightarrow$ C$_2$H$_4$(2S)	Reversible
R3	C$_2$H$_4$(2S) + O(S) $\rightarrow$ CH$_3$CHO(2S) + Pt(S)	
R4	CH$_3$CHO(2S) + O(S) $\rightarrow$ CH$_3$COOH(2S) + Pt(S)	
R5	CH$_3$COOH(2S) + O(S) $\rightarrow$ CH$_3$(S) + OH(S)+ CO$_2$(S)	
R6	CH$_3$(S) + O(S) $\rightarrow$ CH$_2$(S) + OH(S)	
R7	CH$_2$(S) + O(S) $\rightarrow$ CH(S) + OH(S)	
R8	CH(S) + O(S) + OH(S) $\rightarrow$ CO(S) + Pt(S)+ H$_2$O(S)	
R9	CO(S) + O(S) $\rightarrow$ CO$_2$(S) + Pt(S)	
R10	H$_2$O(S) $\leftrightarrow$ H$_2$O + Pt(S)	Reversible
R11	CO$_2$(S) $\leftrightarrow$ CO$_2$ + Pt(S)	Reversible
R12	CO(S) $\leftrightarrow$ CO + Pt(S)	Reversible

Note: "(S)" stands for exposed Pt active sites, and X(S) means that the "X" molecule was adsorbed on Pt active sites.

γ-Al$_2$O$_3$ was inert and not reducible. It was not anticipated that the reaction, which only affected Pt, would take place at the surface of such support surfaces. The C$_2$H$_4$ oxidation process (Table 2) had been suggested for these Pt/γ-Al$_2$O$_3$ catalysts' non-reducible support. The MvK-type reaction on supported-Pt catalysts was demonstrated by FT-IR observations, which showed the synthesis of intermediates after supported-Pt was exposed to C$_2$H$_4$ gas at 180 °C (Figure 5). This observation validated the reaction mechanism. An indication that C$_2$H$_4$ and O$_2$ were adsorbed on Pt and underwent the redox reaction, for instance, was the existence of Pt-OH, =C-H, -CH$_3$, and -CH$_2$ species (Figure 5).

3.4. Identification of Active Sites by In-Situ DRIFTS

Supported noble metal-based catalysts, primarily Pt, have undergone substantial research for the reactions in recent years due to their remarkable activity and stability at low reaction temperatures. On the other side, there was an ongoing dispute on the reaction mechanisms, especially regarding active site constructions (single atoms versus small Pt nanoparticles). Understanding the C$_2$H$_4$ oxidation mechanism would advance significantly with direct observation of the catalytic performance of certain sites that offered statistically sufficient information on on-site identification and quantification, as well as activity evaluation. Using infrared (IR) technology, single-atom Pt and Pt nanoparticles could be distinguished and quantified quickly and easily. The use of IR spectra of CO

on supported noble metal catalysts is particularly common because of its sensitivity to the atomic and electronic structural architectures of the binding sites [43,44]. The IR peaks in the polycarbonyl region could be attributed to CO molecules that have Pt atoms adsorbed on single atom and nanoparticle surfaces ($>2100 \, cm^{-1}$) and surfaces ($<2100 \, cm^{-1}$), respectively [43].

Figures 6 and 7 showed the in situ DRIFTS spectra of C_2H_4 oxidation on PtAl-NF and PtAl-NW and the corresponding IR intensities of CO as a function of the temperature, respectively. It was found that the PtAl-NF remained almost unchanged when the temperature was raised from 120 °C to 180 °C, indicating that the single-atom Pt ($2102 \, cm^{-1}$) indeed lacked catalytic activity for the CO intermediates (Figure 6). Moreover, there were no characteristic peaks ($<2100 \, cm^{-1}$) that originated from CO molecules adsorbed on Pt nanoparticles, thereby implying that Pt nanoparticles (~1 nm) could oxide CO and then desorb as CO_2 at a reaction temperature above 120 °C. However, as C_2H_4 was oxidized with PtAl-NW catalyst at elevated temperature (Figure 7), the peaks corresponding to Pt nanoparticles ($2040 \, cm^{-1}$) appeared but were reduced in intensity. The appearance of the peak could be ascribed to a higher proportion of <1 nm Pt nanoparticles on PtAl-NW as shown in Figure 8c. Because the smaller Pt particles (<1 nm) indicated lower coordination of Pt and led to stronger interactions between Pt and CO [46]. The PtAl-NW showed a redshift of around $10 \, cm^{-1}$ in the region $>2100 \, cm^{-1}$, indicating that the CO molecule was adsorbed on Pt species other than a single atom [43]. Compared with 180 °C (Figure 7), the IR peak was red shifted from $2103 \, cm^{-1}$ to $2110 \, cm^{-1}$ at 120 °C because of dipole-dipole coupling between CO molecules. Single-atom Pt and full exposed Pt clusters had similar CO adsorption properties to single-atom Pt because of the similar low coordination [48]. Based on the IR (Figure 7) and HAADF-STEM (Figure 8c) results of PtAl-NW, the IR peaks at $2103 \, cm^{-1}$ to $2110 \, cm^{-1}$ were assigned to CO molecules adsorbed on full exposed Pt clusters.
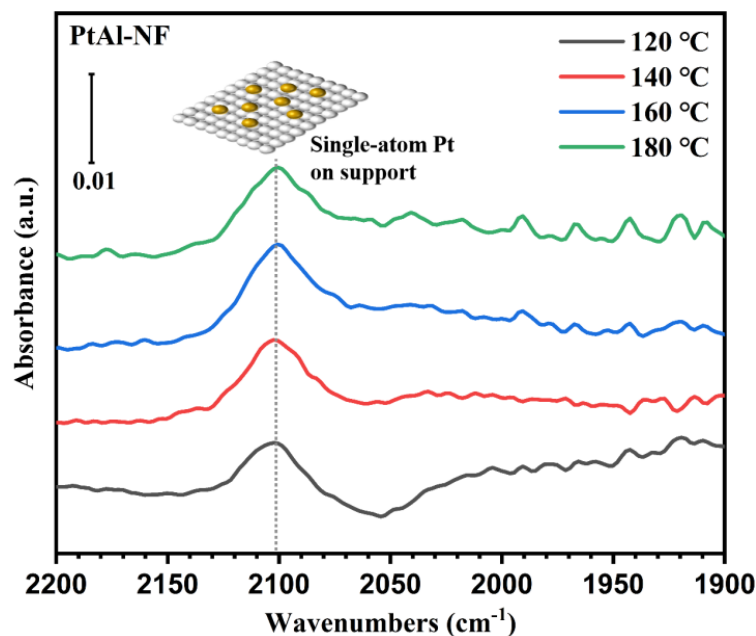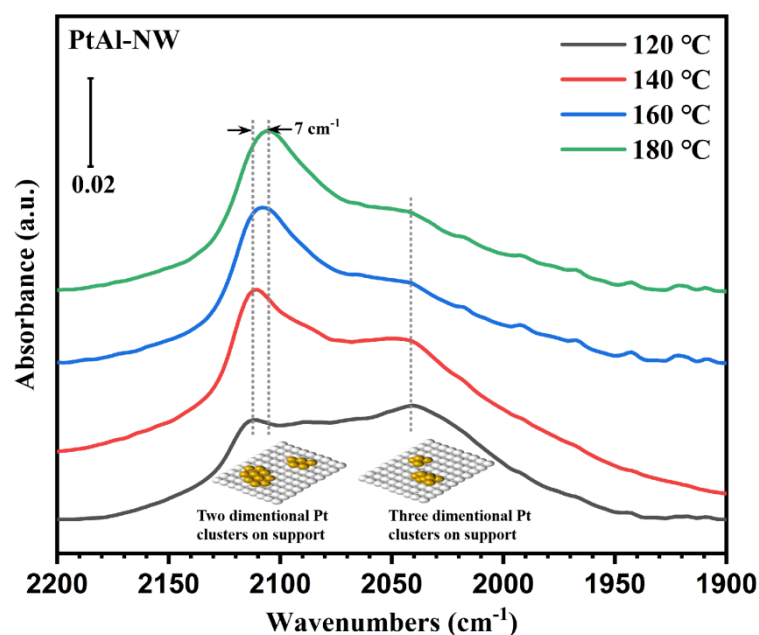

Figure 6. In situ DRIFT spectra over PtAl−NF at temperatures from 120 to 180 °C. Reaction conditions: 700 ppm C_2H_4, 10% O_2, N_2 balance, 17 mg catalyst, and 50 mL min^{-1} flow rate.

Figure 7. In situ DRIFT spectra over PtAl−NW at temperatures from 120 °C to 180 °C. Reaction conditions: 700 ppm C_2H_4, 10% O_2, N_2 balance, 17 mg catalyst, 50 mL min^{-1} flow rate.
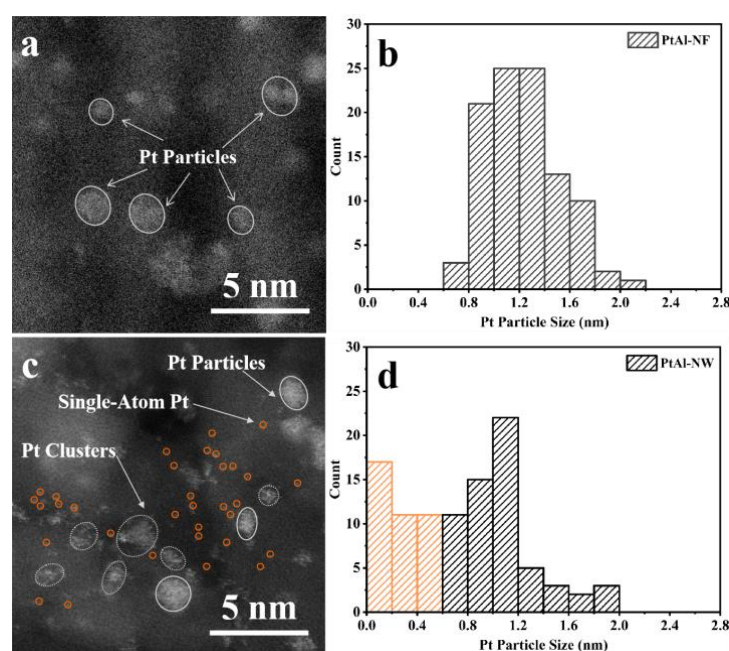

Figure 8. HAADF-STEM images of (**a**) PtAl-NF and (**c**) PtAl-NW; Pt particle size distribution of (**b**) PtAl-NF and (**d**) PtAl-NW. The count number of Pt particles on each sample was 100.

The IR spectra were collected in a reaction mixture of 0.07 vol. % C_2H_4 and 20 vol. % O_2 from 120 °C to 180 °C on PtAl-NF and PtAl-NW catalysts. The Pt surface could only exist in two stable states: CO-covered (inactive) or O-covered (active), hence the limiting step mostly prevented the C_2H_4 oxidation (reaction R9 in Table 2). Pt agglomerates with various structural variations, including single-atom Pt, full-exposure Pt clusters, and Pt nanoparticles, displayed varying CO oxidation activities, as shown in Figure 7. According to the Bronsted-Evans-Polanyi relations, Pt nanoparticles (<1 nm), single-atom Pt, and fully exposed Pt had larger CO oxidation barriers, raising the ignition temperature (Figure 4) and lowering CO tolerance (Figure 7). Pt nanoparticles (~1 nm) supplied Pt sites that were simple to set up in a Pt-O active state, allowing CO to be swiftly converted into CO_2.

3.5. Structures of Pt Supported on γ-Al_2O_3

By using high-angle annular dark-field scanning transmission electron microscopy, the morphology and Pt particle size distribution of the samples (PtAl-NF and PtAl-NW) were observed and have been shown in Figure 8. White ellipses show that Pt nanoparticles were evenly dispersed on the alumina surface of PtAl-NF, with an average particle size distribution of about 1.2 nm (Figures 8a and 3b). There were hardly any clusters of single Pt atoms (individual Pt atoms in the agglomerates). On PtAl-NW, however, single-atom Pt, Pt clusters, and Pt nanoparticles were seen in the 0–2 nm range, as shown in Figure 8c. Figure 8d showed that PtAl-NW had a narrower Pt particle size distribution in comparison to PtAl-NW, indicating an improved Pt dispersion and excellent atomic utilization. It may be emphasized that the Pt clusters and single atoms showed virtually perfectly dispersion of Pt atoms across the Al-NW surface. Additionally, the yellow bins in Figure 8d represent the 39% count of single-atom Pt and Pt clusters. As previously explained [49], Pt was evenly dispersed across the surface of the alumina (100 facets). Pt preferred to be anchored on the (100) facets of the γ-Al_2O_3 surface at the coordinatively unsaturated Al^{3+} sites, where the formation of full exposed Pt clusters furnished the energetically most stable overlayer structure.

3.6. Electronic Properties of Pt/γ-Al_2O_3

To investigate the existing valence states of Pt element on Pt/γ-Al_2O_3 and determine their relationship with their catalytic characteristics, XPS examinations of the catalysts were carried out (Figure 9). Pt 4d experiments were carried out, and the deconvoluted spectra of Pt 4d were obtained. After Gaussian (80%)-Lorentzian (20%) fitting, Pt 4d spectra for both samples were found to comprise two primary doublets reflecting two distinct Pt states. The distinctive peaks of Pt^0 were assigned to the binding energy of Pt $4d_{5/2}$ at 315.8 eV, whereas the signal at the higher range of 317.8 eV–318.9 eV belonged to $Pt^{\delta+}$ [45]. Furthermore, when the agglomerates decreased, the binding energy of Pt 4d increased, which was in good agreement with the results of HAADF-STEM characterization. The CO band in IR spectra ascribed to $Pt^{\delta+}$-CO with higher binding energy (PtAl-NW), was redshifted compared to the absorption band from lower binding energy $Pt^{\delta+}$ (PtAl-NF), presumably because of the Pt d-electron back-donation to the CO π^* anti-bonding orbital [44]. The PtAl-NW catalyst clearly included 46.3% $Pt^{\delta+}$ (318.9 eV) and 53.7% Pt^0 (315.8 eV), whereas the PtAl-NF catalyst had 38.1% $Pt^{\delta+}$ (317.8 eV) and 61.9% Pt^0 (315.8 eV). It was found that the Pt states of the PtAl-NF catalyst were more electron-rich than those of the PtAl-NW catalyst and maintained the metallic Pt^0 state, resulting in a smaller abundance of CO-covered Pt sites (inactive) and a higher abundance of O-covered Pt sites (active) on the surface.

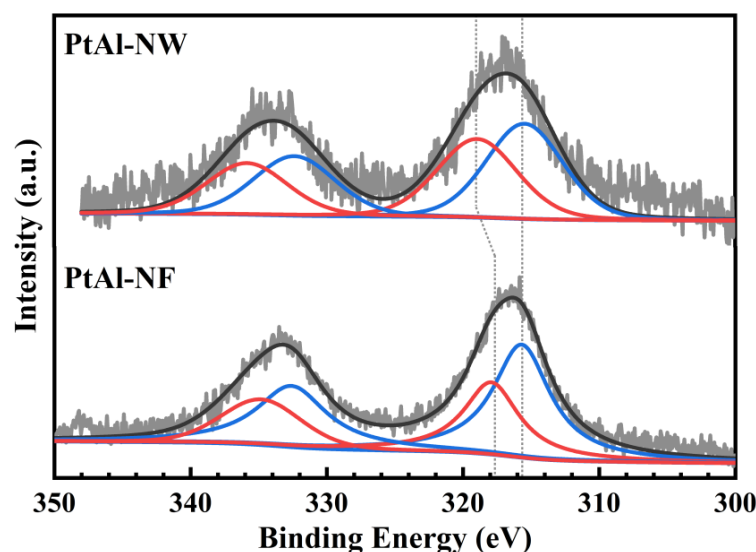

Figure 9. XPS Pt 4d spectra of PtAl-NF and PtAl-NW.

4. Conclusions

In this study, subnanometer and nanometer scale Pt nanoparticles, single-atom Pt, and full exposed Pt clusters supported on γ-Al$_2$O$_3$ were investigated as the active Pt sites for C$_2$H$_4$ oxidation. Pt-γ-Al$_2$O$_3$ interaction was morphology-dependent, and different states of Pt species could be furnished in this manner. A simple surface reaction mechanism was proposed based on surface species measurements. The 1 nm Pt nanoparticles on γ-Al$_2$O$_3$ exhibited a much higher activity than subnanometer particles and full exposed Pt clusters. The XPS results clearly showed that Pt supported on PtAl-NF had a higher ratio (61.9%) of Pt^0 and a lower binding energy Pt$^{\delta+}$ (317.8 eV) than PtAl-NW, which indicated that CO (intermediates) adsorbed on Pt sites had a lower oxidation barrier and are conveniently converted to easily desorbed CO$_2$ (R9). There are, thus, few CO-poisoned Pt sites and high reaction rates. Furthermore, γ-Al$_2$O$_3$ with (110) and (100) basal planes resulted in various Pt morphology and dispersion, and (100) facets preferred to adsorb H$_2$O molecules leading to the occupation of Pt active sites by H$_2$O. Our results demonstrate that Pt with more dispersion (subnanometer particles, fully exposed Pt clusters, and single-atom Pt) has a higher material use efficiency, although there is still room to improve activity per Pt atom. According to the findings, increased atom utilization does not necessarily lead to an ideal catalytic performance when the noble metal loading is constant.

Novelty Statement: In this work, the structure sensitivity and valence states of supported Pt species, ranging from single-atom sites to cluster (sub 1 nm) and 1–2 nm nanoparticles have been investigated for the C$_2$H$_4$ oxidation by in situ DRIFTS. This study showed that the 1 nm Pt nanoparticles on γ-Al$_2$O$_3$ exhibited a much higher activity than subnanometer particles, full exposed Pt clusters, and single-atom Pt. Our findings show that greater Pt dispersion (subnanometer particles, full exposed Pt clusters, and single-atom Pt) has an increased material use efficiency, but there is still space to enhance activity per Pt atom. The results imply that when the noble metal loading remains constant, increasing atom usage does not always result in optimum catalytic performance.

References

1. Huang, R.J.; Zhang, Y.; Bozzetti, C.; Ho, K.F.; Cao, J.J.; Han, Y.; Daellenbach, K.R.; Slowik, J.G.; Platt, S.M.; Canonaco, F.; et al. High secondary aerosol contribution to particulate pollution during haze events in China. *Nature* **2014**, *514*, 218–222. [CrossRef] [PubMed]

2. Zhang, Q.; Zheng, Y.; Tong, D.; Shao, M.; Wang, S.; Zhang, Y.; Xu, X.; Wang, J.; He, H.; Liu, W.; et al. Drivers of improved PM2.5 air quality in China from 2013 to 2017. *Proc. Natl. Acad. Sci. USA* **2019**, *116*, 24463–24469. [CrossRef] [PubMed]

3. Li, M.; Zhang, Q.; Zheng, B.; Tong, D.; Lei, Y.; Liu, F.; Hong, C.; Kang, S.; Yan, L.; Zhang, Y.; et al. Persistent growth of anthropogenic non-methane volatile organic compound (NMVOC) emissions in China during 1990–2017: Drivers, speciation and ozone formation potential. *Atmos. Chem. Phys.* **2019**, *19*, 8897–8913. [CrossRef]

4. Peng, S.; Li, W.; Deng, Y.; Li, W.; Ma, X.; Chen, Y. Removal of low concentration CH_3SH with regenerable Cu-doped mesoporous silica. *J. Colloid Interface Sci.* **2018**, *513*, 903–910. [CrossRef]

5. Cappelletti, M.; Fedi, S.; Frascari, D.; Ohtake, H.; Turner, R.J.; Zannoni, D. Analyses of both the *alkB* gene transcriptional start site and *alkB* promoter-inducing properties of *Rhodococcus* sp. strain BCP1 grown on n-alkanes. *Appl. Environ. Microbiol.* **2011**, *77*, 1619–1627. [CrossRef]

6. Zhang, X.H.; Liu, Q.L.; Xiong, Y.; Zhu, A.M.; Chen, Y.; Zhang, Q.G. Pervaporation dehydration of ethyl acetate/ethanol/water azeotrope using chitosan/poly (vinyl pyrrolidone) blend membranes. *J. Membr. Sci.* **2009**, *327*, 274–280. [CrossRef]

7. Sun, W.; Shao, M.; Granier, C.; Liu, Y.; Ye, C.S.; Zheng, J.Y. Long-Term Trends of Anthropogenic SO_2, NOx, CO, and NMVOCs Emissions in China. *Earth's Future* **2018**, *6*, 1112–1133. [CrossRef]

8. Huang, H.; Xu, Y.; Feng, Q.; Leung, D.Y.C. Low temperature catalytic oxidation of volatile organic compounds: A review. *Catal. Sci. Technol.* **2015**, *5*, 2649–2669. [CrossRef]

9. He, C.; Cheng, J.; Zhang, X.; Douthwaite, M.; Pattisson, S.; Hao, Z. Recent Advances in the Catalytic Oxidation of Volatile Organic Compounds: A Review Based on Pollutant Sorts and Sources. *Chem. Rev.* **2019**, *119*, 4471–4568. [CrossRef]

10. Zhao, J.; Xi, W.J.; Tu, C.S.; Dai, Q.G.; Wang, X.Y. Catalytic oxidation of chlorinated VOCs over Ru/Ti_xSn_{1-x} catalysts. *Appl. Catal. B* **2020**, *263*, 18237. [CrossRef]

11. Xue, T.; Li, R.; Gao, Y.; Wang, Q. Iron mesh-supported vertically aligned Co-Fe layered double oxide as a novel monolithic catalyst for catalytic oxidation of toluene. *Chem. Eng. J.* **2020**, *384*, 123284. [CrossRef]

12. Singh, S.A.; Madras, G.; Sreedhar, I. Transition Metal (Ni, Cu and Fe) Substituted Co_3O_4–ZrO_2 Catalysts for Lean Methane Combustion. *Top. Catal.* **2020**, *64*, 243–255. [CrossRef]

13. Naing, S.; Kristyawan, I.P.A.; Murakami, H.; Hinokuma, S.; Matsumoto, Y.; Omori, T.; Wang, Y.; Yokohata, H.; Kawano, M.; Takebayashi, H.; et al. Development of Detailed Surface Reaction Mechanism of $C_2H_4/C_{(3)}H_{(6)}$ Oxidation on $Pt/Al_{(2)}O_{(3)}$ Monolith Catalyst Based on Gas Phase and Surface Species Analyses. *Combust. Sci. Technol.* **2020**, *194*, 1458–1480. [CrossRef]

14. Khan, H.A.; Hao, J.Y.; Farooq, A. Catalytic performance of Pd catalyst supported on Zr:Ce modified mesoporous silica for methane oxidation. *Chem. Eng. J.* **2020**, *397*, 125489. [CrossRef]

15. Yang, A.C.; Zhu, H.; Li, Y.; Cargnello, M. Support Acidity Improves Pt Activity in Propane Combustion in the Presence of Steam by Reducing Water Coverage on the Active Sites. *ACS Catal.* **2021**, *11*, 6672–6683. [CrossRef]

16. Gan, T.; Chu, X.F.; Qi, H.; Zhang, W.X.; Zou, Y.C.; Yan, W.F.; Liu, G. Pt/Al_2O_3 with ultralow Pt-loading catalyze toluene oxidation: Promotional synergistic effect of Pt nanoparticles and Al_2O_3 support. *Appl. Catal. B* **2019**, *257*, 17943. [CrossRef]

17. Kim, J.; Kim, Y.; Wiebenga, M.H.; Oh, S.H.; Kim, D.H. Oxidation of C_3H_8, iso-C_5H_{12} and C_3H_6 under near-stoichiometric and fuel-lean conditions over aged $Pt-Pd/Al_2O_3$ catalysts with different Pt:Pd ratios. *Appl. Catal. B* **2019**, *251*, 283–294. [CrossRef]

18. Weon, S.; Huang, D.; Rigby, K.; Chu, C.; Wu, X.; Kim, J.H. Environmental Materials beyond and below the Nanoscale: Single-Atom Catalysts. *ACS EST Eng.* **2020**, *1*, 157–172. [CrossRef]

19. Lang, R.; Du, X.; Huang, Y.; Jiang, X.; Zhang, Q.; Guo, Y.; Liu, K.; Qiao, B.; Wang, A.; Zhang, T. Single-Atom Catalysts Based on the Metal-Oxide Interaction. *Chem. Rev.* **2020**, *120*, 11986–12043. [CrossRef]

20. Zhang, T.; Walsh, A.G.; Yu, J.; Zhang, P. Single-atom alloy catalysts: Structural analysis, electronic properties and catalytic activities. *Chem. Soc. Rev.* **2021**, *50*, 569–588. [CrossRef]

21. Moses-DeBusk, M.; Yoon, M.; Allard, L.F.; Mullins, D.R.; Wu, Z.; Yang, X.; Veith, G.; Stocks, G.M.; Narula, C.K. CO oxidation on supported single Pt atoms: Experimental and ab initio density functional studies of CO interaction with Pt atom on theta-$Al_2O_3(010)$ surface. *J. Am. Chem. Soc.* **2013**, *135*, 12634–12645. [CrossRef] [PubMed]

22. Qiao, B.; Liang, J.X.; Wang, A.; Xu, C.Q.; Li, J.; Zhang, T.; Liu, J.J. Ultrastable single-atom gold catalysts with strong covalent metal-support interaction (CMSI). *Nano Res.* **2015**, *8*, 2913–2924. [CrossRef]

23. Chen, J.; Wanyan, Y.; Zeng, J.; Fang, H.; Li, Z.; Dong, Y.; Qin, R.; Wu, C.; Liu, D.; Wang, M.; et al. Surface Engineering Protocol To Obtain an Atomically Dispersed Pt/CeO_2 Catalyst with High Activity and Stability for CO Oxidation. *ACS Sustain. Chem. Eng.* **2018**, *6*, 14054–14062. [CrossRef]

24. DeRita, L.; Dai, S.; Lopez-Zepeda, K.; Pham, N.; Graham, G.W.; Pan, X.; Christopher, P. Catalyst Architecture for Stable Single Atom Dispersion Enables Site-Specific Spectroscopic and Reactivity Measurements of CO Adsorbed to Pt Atoms, Oxidized Pt Clusters, and Metallic Pt Clusters on TiO_2. *J. Am. Chem. Soc.* **2017**, *139*, 14150–14165. [CrossRef]

25. Dong, C.; Gao, Z.; Li, Y.; Peng, M.; Wang, M.; Xu, Y.; Li, C.; Xu, M.; Deng, Y.; Qin, X.; et al. Fully exposed palladium cluster catalysts enable hydrogen production from nitrogen heterocycles. *Nat. Catal.* **2022**, *5*, 485–493. [CrossRef]

26. Li, L.; Jiang, Y.F.; Zhang, T.; Cai, H.; Zhou, Y.; Lin, B.; Lin, X.; Zheng, Y.; Zheng, L.; Wang, X.; et al. Size sensitivity of supported Ru catalysts for ammonia synthesis: From nanoparticles to subnanometric clusters and atomic clusters. *Chem* **2021**, *8*, 749–768. [CrossRef]

27. Chen, S.; Li, S.; You, R.; Guo, Z.; Wang, F.; Li, G.; Yuan, W.; Zhu, B.; Gao, Y.; Zhang, Z.; et al. Elucidation of Active Sites for CH_4 Catalytic Oxidation over Pd/CeO_2 Via Tailoring Metal–Support Interactions. *ACS Catal.* **2021**, *11*, 5666–5677. [CrossRef]

28. Zhang, X.; Cui, W.W.; Page, K.L.; Pearce, C.I.; Bowden, M.E.; Graham, T.R.; Shen, Z.Z.; Li, P.; Wang, Z.M.; Kerisit, S.; et al. Size and Morphology Controlled Synthesis of Boehmite Nanoplates and Crystal Growth Mechanisms. *Cryst. Growth Des.* **2018**, *18*, 3596–3606. [CrossRef]

29. Jiao, W.; Wu, X.; Xue, T.; Li, G.; Wang, W.; Wang, Y.; Wang, Y.; Tang, Y.; He, M.Y. Morphological Controlled Growth of Nanosized Boehmite with Enhanced Aspect Ratios in an Organic Additive-Free Cationic-Anionic Double Hydrolysis Method. *Cryst. Growth Des.* **2016**, *16*, 5166–5173. [CrossRef]

30. Chen, X.Y.; Huh, H.S.; Lee, S.W. Hydrothermal synthesis of boehmite (gamma-AlOOH) nanoplatelets and nanowires: pH-controlled morphologies. *Nanotechnology* **2007**, *18*, 285608. [CrossRef]

31. Kuiry, S.C.; Megen, E.; Patil, S.D.; Deshpande, S.A.; Seal, S. Solution-based chemical synthesis of boehmite nanofibers and alumina nanorods. *J. Phys. Chem. B* **2005**, *109*, 3868–3872. [CrossRef]

32. Xu, S.; Jaegers, N.R.; Hu, W.; Kwak, J.H.; Bao, X.; Sun, J.; Wang, Y.; Hu, J.Z. High-Field One-Dimensional and Two-Dimensional ^{27}Al Magic-Angle Spinning Nuclear Magnetic Resonance Study of theta-, delta-, and gamma-Al_2O_3 Dominated Aluminum Oxides: Toward Understanding the Al Sites in gamma-Al_2O_3. *ACS Omega* **2021**, *6*, 4090–4099. [CrossRef]

33. Liu, Q.; Wang, A.; Wang, X.; Gao, P.; Wang, X.; Zhang, T. Synthesis, characterization and catalytic applications of mesoporous gamma-alumina from boehmite sol. *Microporous Mesoporous Mater.* **2008**, *111*, 323–333. [CrossRef]

34. Alphonse, P.; Courty, M. Structure and thermal behavior of nanocrystalline boehmite. *Thermochim. Acta* **2005**, *425*, 75–89. [CrossRef]

35. Li, Z.; Liu, G.H.; Li, X.B.; Qi, T.; Peng, Z.H.; Zhou, Q.S. Effects of Cation on the Morphology of Boehmite Precipitated from Alkaline Solutions by Adding Gibbsite as Seed. *Cryst. Growth Des.* **2019**, *19*, 1778–1785. [CrossRef]

36. Cai, W.M.; Zhang, S.G.; Lv, J.G.; Chen, J.C.; Yang, J.; Wang, Y.B.; Guo, X.F.; Peng, L.M.; Ding, W.P.; Chen, Y.; et al. Nanotubular Gamma Alumina with High-Energy External Surfaces: Synthesis and High Performance for Catalysis. *ACS Catal.* **2017**, *7*, 4083–4092. [CrossRef]

37. Krokidis, X.; Raybaud, P.; Gobichon, A.E.; Rebours, B.; Euzen, P.; Toulhoat, H. Theoretical study of the dehydration process of boehmite to gamma-alumina. *J. Phys. Chem. B* **2001**, *105*, 5121–5130. [CrossRef]

38. Chen, X.Y.; Zhang, Z.H.; Li, X.L.; Lee, S.W. Controlled hydrothermal synthesis of colloidal boehmite (gamma-AlOOH) nanorods and nanoflakes and their conversion into gamma-Al_2O_3 nanocrystals. *Solid State Commun.* **2008**, *145*, 368–373. [CrossRef]

39. Kaiser, S.; Maleki, F.; Zhang, K.; Harbich, W.; Heiz, U.; Tosoni, S.; Lechner, B.A.J.; Pacchioni, G.; Esch, F. Cluster Catalysis with Lattice Oxygen: Tracing Oxygen Transport from a Magnetite (001) Support onto Small Pt Clusters. *ACS Catal.* **2021**, *11*, 9519–9529. [CrossRef]

40. Ziemba, M.; Schilling, C.; Ganduglia-Pirovano, M.V.; Hess, C. Toward an Atomic-Level Understanding of Ceria-Based Catalysts: When Experiment and Theory Go Hand in Hand. *Acc. Chem. Res.* **2021**, *54*, 2884–2893. [CrossRef]

41. Gao, X.; Li, Z.; Chen, C.; Da, C.; Liu, L.; Tian, S.; Ji, G. The Determination of Pore Shape and Interfacial Barrier of Entry for Light Gases Transport in Amorphous TEOS-Derived Silica: A Finite Element Method. *ACS Appl. Mater. Interfaces* **2021**, *13*, 4804–4812. [CrossRef]

42. Zaki, M.I.; Hasan, M.A.; Pasupulety, L. Surface Reactions of Acetone on Al_2O_3, TiO_2, ZrO_2, and CeO_2: IR Spectroscopic Assessment of Impacts of the Surface Acid−Base Properties. *Langmuir* **2001**, *17*, 768–774. [CrossRef]

43. Ding, K.; Gulec, A.; Johnson, A.M.; Schweitzer, N.M.; Stucky, G.D.; Marks, L.D.; Stair, P.C. Identification of active sites in CO oxidation and water-gas shift over supported Pt catalysts. *Science* **2015**, *350*, 189–192. [CrossRef]

44. Jeong, H.; Kwon, O.; Kim, B.S.; Bae, J.; Shin, S.; Kim, H.E.; Kim, J.; Lee, H. Highly durable metal ensemble catalysts with full dispersion for automotive applications beyond single-atom catalysts. *Nat. Catal.* **2020**, *3*, 368–375. [CrossRef]

45. Jang, E.J.; Lee, J.; Oh, D.G.; Kwak, J.H. CH_4 Oxidation Activity in Pd and Pt–Pd Bimetallic Catalysts: Correlation with Surface PdOx Quantified from the DRIFTS Study. *ACS Catal.* **2021**, *11*, 5894–5905. [CrossRef]

46. Pramhaas, V.; Roiaz, M.; Bosio, N.; Corva, M.; Rameshan, C.; Vesselli, E.; Grönbeck, H.; Rupprechter, G. Interplay between CO Disproportionation and Oxidation: On the Origin of the CO Reaction Onset on Atomic Layer Deposition-Grown Pt/ZrO_2 Model Catalysts. *ACS Catal.* **2021**, *11*, 208–214. [CrossRef]

47. Dablemont, C.; Lang, P.; Mangeney, C.; Piquemal, J.Y.; Petkov, V.; Herbst, F.; Viau, G. FTIR and XPS Study of Pt Nanoparticle Functionalization and Interaction with Alumina. *Langmuir* **2008**, *24*, 5832–5841. [CrossRef]

48. Peng, M.; Dong, C.; Gao, R.; Xiao, D.; Liu, H.; Ma, D. Fully Exposed Cluster Catalyst (FECC): Toward Rich Surface Sites and Full Atom Utilization Efficiency. *ACS Cent. Sci.* **2020**, *7*, 262–273. [CrossRef] [PubMed]

49. Kwak, J.H.; Hu, J.; Mei, D.; Yi, C.W.; Kim, D.H.; Peden, C.H.; Allard, L.F.; Szanyi, J. Coordinatively Unsaturated Al^{3+} Centers as Binding Sites for Active Catalyst Phases of Platinum on gamma-Al_2O_3. *Science* **2009**, *325*, 1670–1673. [CrossRef] [PubMed]